

# Effects of zigzag edge states on the thermoelectric properties of finite graphene nanoribbons

David Ming Ting Kuo

*Department of Electrical Engineering and Department of Physics,  
National Central University, Chungli, 320 Taiwan*

(Dated: May 3, 2022)

Thermoelectric properties of finite graphene nanoribbons (GNRs) coupled to metallic electrodes are theoretically studied in the framework of tight-binding model and Green's function approach. When the zigzag sides are coupled to the electrodes, the electron transport through the localized edge states can occur only if the channel length between electrodes is smaller than the decay length of these localized zigzag edge states. When the armchair edges are coupled to the electrodes, there is an interesting thermoelectric behavior associated with the mid-gap states when the GNR is in the semiconducting phase. Here we show that the thermoelectric behavior of zigzag edge states of GNRs with armchair sides connected to electrodes is similar to that of two parallel quantum dots with similar orbital degeneracy. Furthermore, it is demonstrated that the electrical conductance and power factor given by the zigzag edge states are quite robust against the defect scattering.

## I. INTRODUCTION

The efficiency of thermoelectric materials is determined by the dimensionless figure of merit  $ZT = S^2 G_e T / (\kappa_e + \kappa_{ph})$ , which depends on the Seebeck coefficient ( $S$ ), electrical conductance ( $G_e$ ) and thermal conductance ( $\kappa = \kappa_e + \kappa_{ph}$ ) of the material.<sup>1,2)</sup> The thermal conductance includes contributions due to electron transport ( $\kappa_e$ ) and phonon transport ( $\kappa_{ph}$ ). Here,  $T$  denotes the equilibrium temperature of the thermoelectric device. For applications of thermoelectric devices, not only the thermoelectric efficiency but also the electrical power output need to be optimized. However, there is often a trade off between the efficiency and power output in conventional thermoelectric materials.<sup>2)</sup> For example, with the increase of  $G_e$  one often faces the increase of  $\kappa_e$  and reduction of  $S$ . As a result  $ZT$  is reduced.

To find the best compromise between thermoelectric efficiency and electrical power output, Hicks and Dresselhaus theoretically demonstrated that the thermoelectric performance can be significantly enhanced in low-dimensional systems due to the reduced  $\kappa_{ph}$ .<sup>3)</sup> For quasi one dimensional systems,  $\kappa_{ph}$  can be highly reduced meanwhile the power factor,  $PF = S^2 G_e$  could remain similar to that of bulk materials due to the enhancement of  $S$ .<sup>4)</sup> Nanowires with high thermoelectric efficiency have been reported in several theoretical and experimental studies.<sup>4-8)</sup> Nevertheless, these quasi one-dimensional nanowires have about a few hundred atoms in the cross-sectional area with diameter of 10 nm for the carrier transport.<sup>4-8)</sup> The fabrication of one-dimensional (1D) solid state system with smaller cross-section was a challenging problem in material science. The discovery of two-dimensional (2D) graphene in 2004 opened the door for realizing 1D systems with small cross-section,<sup>9)</sup> since one can atomically precise fabricate graphene nanoribbons (GNRs) by bottom-up approach.<sup>10)</sup> Graphene with a hexagonal lattice structure is a zero-gap semiconductor because its conduction and valence bands meet at the Dirac points.<sup>11)</sup> Although such a zero-gap property lim-

its its applications in electronics and optoelectronics, the discovery of 2D graphene stimulates an impressive development of 2D materials with semiconducting properties.

In recent years, tremendous efforts have been devoted to the investigation of the transport and optical properties of 2D materials for applications of new generation electronics and optoelectronics.<sup>12-21)</sup> For nanowires realized by 2D materials, it is expected that their thermal conductances will be dramatically reduced owing to the small number of atoms in the cross section.<sup>22-25)</sup> Compared with nanoribbons made from other two-dimensional material, GNRs are easier to obtain.<sup>10,26,27)</sup> Meanwhile, recycling carbons plays an important role to eternal development of the earth. Therefore, it is desirable to clarify the transport and thermoelectric properties of GNRs.<sup>22,28,29)</sup> GNRs have zigzag GRNs (ZGRNs) and armchair GRNs (AGNRs). Because AGNRs exhibit semiconductor phases, most theoretical studies have focused on thermoelectric performance of AGRNs.<sup>22,28,29)</sup> When the zigzag sides of an infinitely long AGRNs are coupled to the electrodes, electron transport through the zigzag-edge states is suppressed due to their localize wave functions.<sup>30-36)</sup> For finite-size GNRs, there exists quantum-confinement effect which depends on whether the short sides of the GNR have zigzag or armchair edges. For experimentally studied AGRNs, the edge states are always present and such a study could provide more insight into the transport characteristics. Size effects on electronic structures of finite-size GNRs have been studied theoretically,<sup>37,38)</sup> however the investigation of their thermoelectrical properties is still lacking.

Here we theoretically investigate the transport and thermoelectric properties of finite size GNRs coupled to the metallic electrodes with two kinds of geometries as shown in Fig. 1. Electron transport is determined not only by GRN types but also their contact geometries. The finite size GNRs in the configuration as shown in Fig. 1(b) could provide a sharp transmission coefficient locating at middle of band gap, which is created by zigzag edges of GNRs. The main goal of this study is to illus-

trate how zigzag edge states to influence the thermoelectric properties of GNRs.

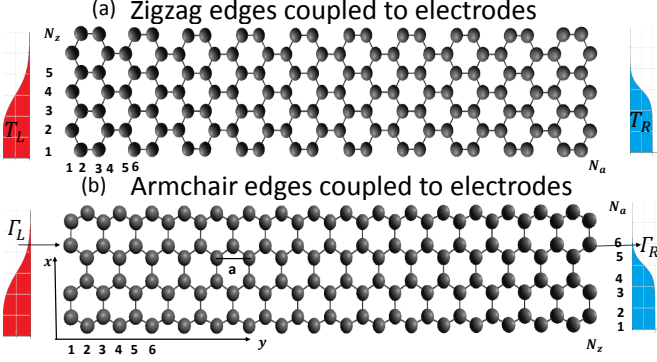


FIG. 1: Schematic diagram of a finite graphene coupled to metallic electrodes.  $\Gamma_L$  ( $\Gamma_R$ ) denotes the tunneling rate of the electrons between the left (right) electrode and the leftmost (rightmost) atoms of a finite graphene nanoribbon.  $T_L$  and  $T_R$  denote the temperature of the left and the right electrodes, respectively. (a) and (b) show the geometry with the zigzag and armchair edges coupled to the electrodes, respectively. The lattice constant of graphene is  $a = 2.46\text{\AA}$ .

## II. FORMALISM

The hexagonal crystal structure of graphene results from the  $\sigma$  bonding formed by  $sp^2$  hybridized orbitals, while the  $p_z$  orbitals form the  $\pi$  bands that play an important role for electron transport near Fermi energy.<sup>30–36</sup> Similar to benzene,<sup>39</sup> it is expected that the  $\sigma$  bands of graphene are well separated from the  $\pi$  bands. Therefore, it is a good approximation to employ a tight-binding model with one  $p_z$  orbital per atomic site to describe the electronic states near the Fermi level of a GNR.<sup>31</sup> To model the thermoelectric properties of a GNR connected to the electrodes, the Hamiltonian of the system depicted in Fig. 1(a) is written as  $H = H_0 + H_{GNR}$ ,<sup>40</sup> where

$$H_0 = \sum_k \epsilon_k a_k^\dagger a_k + \sum_k \epsilon_k b_k^\dagger b_k + \sum_\ell \sum_k V_{k,\ell,j}^L d_{\ell,j}^\dagger a_k + \sum_\ell \sum_k V_{k,\ell,j}^R d_{\ell,j}^\dagger b_k + h.c. \quad (1)$$

The first two terms of Eq. (1) describe the free electrons in the left and right metallic electrodes.  $a_k^\dagger$  ( $b_k^\dagger$ ) creates an electron of with momentum  $k$  and energy  $\epsilon_k$  in the left (right) electrode.  $V_{k,\ell,j=1}^L$  ( $V_{k,\ell,j=N_a}^R$ ) describes the coupling between the left (right) lead with its adjacent atom in the  $\ell$ -th row.

$$H_{GNR} = \sum_{\ell,j} E_{\ell,j} d_{\ell,j}^\dagger d_{\ell,j} + \sum_{\ell,j} \sum_{\ell',j'} t_{(\ell,j),(\ell',j')} d_{\ell,j}^\dagger d_{\ell',j'} + h.c., \quad (2)$$

where  $E_{\ell,j}$  is the on-site energy for the  $p_z$  orbital in the  $\ell$ -th row and  $j$ -th column. Here, the spin-orbit interaction is neglected.  $d_{\ell,j}^\dagger$  ( $d_{\ell,j}$ ) creates (destroys) one electron at the atom site labeled by  $(\ell,j)$  where  $\ell$  and  $j$ , respectively are the row and column indices as illustrated in Fig. 1.  $t_{(\ell,j),(\ell',j')}$  describes the electron hopping energy from site  $(\ell,j)$  to site  $(\ell',j')$ . The electron wave functions of the zigzag edge states of GNRs are well localized,<sup>30–32</sup> and the Coulomb repulsion between two zigzag edge-state electrons can be strong when they are close. Thus, the Coulomb repulsion effect on electron transport through the edge states can be significant when the average occupancy of each site is larger than 0.5 in steady state.<sup>41</sup> On the other hand, the wave functions of the electrons in the bulk-like states are delocalized; hence their weak electron Coulomb interactions can be neglected. Because the transport behavior of zigzag edge states behaves like that of coupled quantum dots (to be demonstrated in the next section), its behavior can be analyzed by considering the Coulomb blockade effect in coupled quantum dots with orbital or valley degeneracy.<sup>41</sup> The tight-binding parameters used for GNR is  $E_{\ell,j} = 0$  and  $t_{(\ell,j),(\ell',j')} = t_{pp\pi} = -2.7\text{ eV}$  for nearest-neighbor hopping only.

To study the transport properties of a GNR junction connected to electrodes, it is convenient to use the Keldysh-Green's function technique.<sup>40,42</sup> Electron and heat currents leaving the electrodes can be expressed as

$$J = \frac{g_s e}{h} \int d\varepsilon \mathcal{T}_{LR}(\varepsilon) [f_L(\varepsilon) - f_R(\varepsilon)], \quad (3)$$

and

$$Q_{e,L(R)} = \frac{\pm g_s e}{h} \int d\varepsilon \mathcal{T}_{LR}(\varepsilon) (\varepsilon - \mu_{L(R)}) [f_L(\varepsilon) - f_R(\varepsilon)] \quad (4)$$

where  $g_s = 2$  denotes the spin degeneracy.  $f_\alpha(\varepsilon) = 1/\{\exp[(\varepsilon - \mu_\alpha)/k_B T_\alpha] + 1\}$  denotes the Fermi distribution function for the  $\alpha$ -th electrode, where  $\mu_\alpha$  and  $T_\alpha$  are the chemical potential and the temperature of the  $\alpha$  electrode.  $e$ ,  $h$ , and  $k_B$  denote the electron charge, the Planck's constant, and the Boltzmann constant, respectively.  $\mathcal{T}_{LR}(\varepsilon)$  denotes the transmission coefficient of a GNR connected to electrodes, which can be solved by the formula  $\mathcal{T}_{LR}(\varepsilon) = 4\text{Tr}[\Gamma_L(\varepsilon)G^r(\varepsilon)\Gamma_R(\varepsilon)G^a(\varepsilon)]$ ,<sup>43,44</sup> where  $(\Gamma_L(\varepsilon)$  and  $\Gamma_R(\varepsilon))$  denote the tunneling rate at the left and right leads, and  $G^r(\varepsilon)$  and  $G^a(\varepsilon)$  are the retarded and advanced Green's function of the GNR. Note that both the Green's functions and the tunneling rates in the transmission coefficient  $\mathcal{T}_{LR}(\varepsilon)$  of Eqs. (3) and (4) are matrices.  $\Gamma_\alpha(\varepsilon) = -\text{Im}(\Sigma_\alpha^r(\varepsilon))$  result from the imaginary part of self energies determined by  $V_{k,\ell,j=1}^L$  and  $V_{k,\ell,j=N_a}^R$  (see Fig. 1(a)). Therefore, the matrix form of  $\Gamma_L(\varepsilon)$  is always different from that of  $\Gamma_R(\varepsilon)$ . For metals such as gold, the density of states is approximately constant near the Fermi energy such that the wide-band limit is a good approximation.<sup>43</sup> In the wide-band limit, the  $\Gamma_{L(R)}(\varepsilon)$  are replaced by constant matrices  $\Gamma_{L(R)}$ .

However, only the diagonal entries are non-zero. In the following, we choose a symmetric coupling such that the non-vanishing matrix elements of  $\Gamma_\alpha$  all take the same value  $\gamma_L = \gamma_R = \gamma$ .<sup>43</sup> In the current study, only integers of  $N_a/4$  are considered here. For the case with odd numbers of  $N_a$ , one edge of the GNR will have broken bonds which lead to unwanted dangling-bond states.

In the linear response regime, the electrical conductance ( $G_e$ ), Seebeck coefficient ( $S$ ) and electron thermal conductance ( $\kappa_e$ ) are given by  $G_e = e^2 \mathcal{L}_0$ ,  $S = -\mathcal{L}_1/(eT\mathcal{L}_0)$  and  $\kappa_e = \frac{1}{T}(\mathcal{L}_2 - \mathcal{L}_1^2/\mathcal{L}_0)$  with  $\mathcal{L}_n$  ( $= 0, 1, 2$ ) defined as

$$\mathcal{L}_n = \frac{2}{h} \int d\varepsilon \mathcal{T}_{LR}(\varepsilon) (\varepsilon - \mu)^n \frac{\partial f(\varepsilon)}{\partial \mu}. \quad (5)$$

Here  $f(\varepsilon) = 1/(\exp^{(\varepsilon - \mu)/k_B T} + 1)$  is the Fermi distribution function of electrodes at equilibrium temperature  $T$  and chemical potential  $\mu$ . As for the phonon contribution to the thermal conductivity,  $\kappa_{ph}$ , we adopt the calculated results reported in ref. [45], where the phonon scattering from defects in carbon nanotubes is studied theoretically. As can be seen from Eq. (5), the transmission coefficient,  $\mathcal{T}_{LR}(\varepsilon)$  plays a significant role for electron transport and thermoelectric properties.

### III. RESULTS AND DISCUSSION

#### A. Zigzag edges coupled to the electrodes

##### 1. Graphene nanoribbons with $N_a \gg N_z$

Armchair graphene nanoribbons (AGNRs) can be either metallic (when  $N_z = 3m + 2$ ) or semiconducting (when  $N_z = 3m$  or  $3m + 1$ ).<sup>30</sup> Here  $m$  is an integer. For reference, the calculated electronic band structures of GNRs with infinite length are given in appendix A. For semiconducting cases, the size of the gap is inversely proportional to  $N_z$  (or the width of the AGNR).<sup>31</sup> To examine the thermoelectric properties of GNRs, we have calculated  $G_e$ ,  $S$  and power factor  $PF$  as functions of  $\mu$  for different  $k_B T$  with  $N_a = 100$  (length  $L_a = 10.5\text{nm}$ ) and  $N_z = 24$  (length  $L_z = 2.8\text{nm}$ ) in Fig. 2. Due to the quantum confinement arising from finite  $N_a$  and  $N_z$ , discrete peaks show up in the  $G_e$  spectra. Because the zigzag edge states are localized electronic states that decay exponentially toward the center of the ribbon (see charge density in appendix B. 1), the probability of electrons transport between the electrodes tunneling through zigzag edge states is vanishingly small for a long channel length ( $L_a = 10.5\text{nm}$ ).

As shown in Fig. 2(a) the GNR has an energy gap around  $0.5\text{ eV}$  for  $N_z = 24$  and  $N_a = 100$ , which is slightly larger than that of an infinitely-long AGNR with  $N_z = 24$ . The  $G_e$  peak shows a thermal broadening behavior with respect to temperature. Oscillatory behavior of  $G_e$  can be observed even at  $k_B T = 27\text{meV}$ .

The temperature-dependent maximum Seebeck coefficient ( $|S_{h,max}|$  for hole or  $|S_{e,max}|$  for electron) shows an impressive value inside the gap region<sup>29</sup>. Note that the unit ( $k_B/e$ ) equals to  $86.25\mu\text{V}/K$ . We have  $|S_{h,max}| = |S_{e,max}| = 431\mu\text{V}/K$  for  $k_B T = 27\text{ meV}$ . As seen in Fig. 2, due to the electron-hole symmetry  $G_e(\mu)$  is symmetric while  $S(\mu)$  is antisymmetric with respect to the sign change of  $\mu$ . Thus,  $S$  vanishes at  $\mu = 0$  at any temperature. In Fig. 2,  $G_e$  is smaller than the quantum conductance,  $G_0 = 2e^2/h$ . For thermoelectric devices it is important to optimize the electrical power outputs as well as efficiency. To increase power factor  $PF = S^2 G_e$ , one can increase  $G_e$  by increasing  $N_z$  or tunneling rates. Thus, we consider case  $N_z \gg N_a$  below.

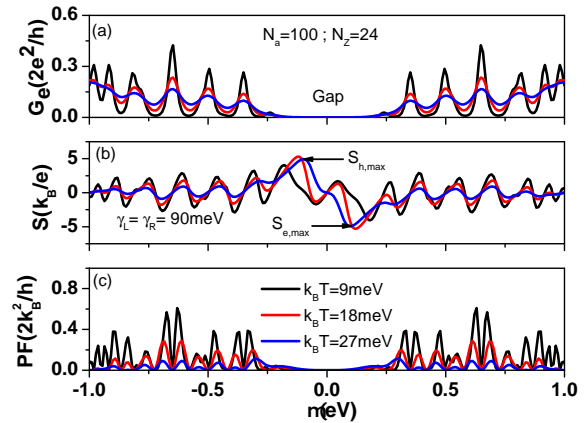


FIG. 2: (a) Electrical conductance  $G_e$ , (b) Seebeck coefficient  $S$  and (c) power factor  $PF$  as functions of  $\mu$  for different temperatures at  $N_a = 100$  ( $L_a = 10.5\text{ nm}$ ) and  $N_z = 24$  ( $L_z = 2.8\text{ nm}$ ). We have adopted electron tunneling rates  $\gamma_L = \gamma_R = 90\text{ meV}$ .

##### 2. Graphene nanoribbons with $N_z \gg N_a$

Figure 3 shows the calculated conductance ( $G_e$ ), Seebeck coefficient ( $S$ ), and power factor ( $PF$ ) of a GNR with  $N_z = 99$  ( $L_z = 12\text{nm}$ ) and  $N_a = 20$  ( $L_a = 1.988\text{nm}$ ) as functions of  $\mu$  for various temperatures. According to Fig. A.2, only zigzag edge states provide tunneling channels between the electrodes when  $|\varepsilon| \leq 1.0\text{eV}$ . Here,  $G_e$  is much enhanced because more carbon atoms of zigzag edges are in contact with the electrodes in this arrangement. The peak at  $\mu = 0$  (marked by  $\Sigma_0$ ) arises from the zigzag edge states. Because zigzag edge states are localized, the width of the  $\Sigma_0$  peak is very sensitive to the  $N_a$  value. In addition, the broadening of  $\Sigma_0$  peak also depends on the tunneling rates,  $\gamma_L$  and  $\gamma_R$ . Here we set  $\gamma_L = \gamma_R = 90\text{ meV}$ . The quantum confinement effect is clearly seen for  $|\mu| \geq 0.2\text{eV}$ . In Fig. 3(b) the maximum Seebeck coefficients are much smaller than  $S_{e(h),max}$  shown in Fig. 2(b). The behavior of Seebeck

coefficient shown in Fig. 3(b) can be described roughly by  $S \approx -\frac{k_B^2 T}{e} \frac{1}{G_e(\mu, T)} \frac{\partial G_e(\mu, T)}{\partial \mu}$ . This implies that the value of  $S$  becomes very small when  $G_e$  is insensitive to  $\mu$ . Fig. 3(c) shows that GNRs give a significant power factor at  $k_B T = 27 \text{ meV}$  as  $\mu$  is tuned away from 0. However, due to large  $\kappa_e$  (not shown here), the thermoelectric efficiency of GNRs in the situation of  $N_z \gg N_a$  is suppressed.

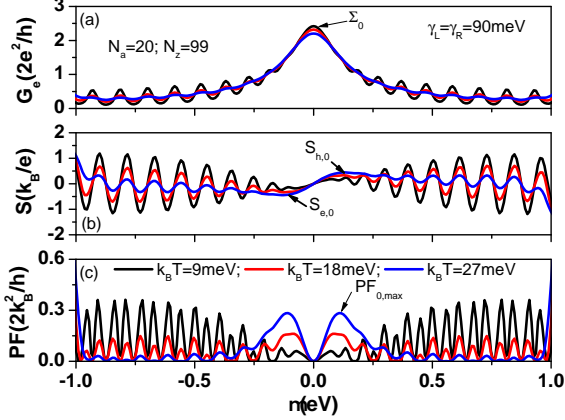


FIG. 3: (a) Electrical conductance  $G_e$ , (b) Seebeck coefficient  $S$  and (c) power factor  $PF$  as functions of  $\mu$  for different temperature values at  $N_a = 20$  ( $L_a = 1.988 \text{ nm}$ ) and  $N_z = 99$  ( $L_z = 12 \text{ nm}$ ).  $\gamma_L = \gamma_R = 90 \text{ meV}$ .

## B. Armchair edges coupled to the electrodes

To further understand the zigzag edge effect on the thermoelectric properties of GNRs, we next consider a GNR with armchair edges coupled to the metallic electrodes (as illustrated in Fig. 1(b)).

### 1. Graphene nanoribbons with $N_z \gg N_a$

In contrast to the situation of Figs. 2 and 3, here we consider the scenario with armchair edges connected to the electrodes. Fig. 4 shows electrical conductance  $G_e$ , Seebeck coefficient  $S$ , power factor  $PF$  and figure of merit  $ZT_e$  as functions of  $\mu$  for various temperatures at  $N_a = 24$  ( $L_a = 2.41 \text{ nm}$ ) and  $N_z = 121$  ( $L_z = 14.76 \text{ nm}$ ). Here we have adopted  $\gamma_{L(R)} = 9 \text{ meV}$  to reduce the broadening effect on  $G_e$  spectra. Since  $N_z \gg N_a$  in this case, the electronic states are comparable to the case of an infinitely-long ZGNR with  $N_a = 24$  (as shown in Fig. A.2). We note that strictly speaking there is always an energy splitting of the pair of zigzag-edge states for ZGNR with finite width, although the splitting can be quite tiny for those edge states with  $|k| > \frac{2\pi}{3a}$ . Thus,

at zero temperature, we find  $G_e(\mu = 0) = 0$ . However, at finite temperature with  $k_B T$  larger than the energy splitting mentioned above, the  $\Sigma_0$  peak in the  $G_e$  spectrum will appear to have a maximum at  $\mu = 0$  due to temperature-smearing effect. When  $\mu$  is tuned away from the zero-energy mode into the fork-shaped region (see Fig. A. 2), the  $G_e$  spectra show a high density of peaks (indicated by  $\Sigma_1$ ) with nearly uniform height, where the spacing between consecutive peaks is approximately  $90 \text{ meV}$ . As seen in Fig. 4(a),  $G_e$  is highly enhanced near  $|\mu| = 0.9 \text{ eV}$ . Such an enhancement of  $G_e$  is attributed to the combination of zigzag-edge states and the second subband. The fast oscillation of  $G_e$  spectra resulting from quantum confinement give rise to significant  $S$  values, which are suppressed as temperature increases. In addition,  $S$  is significantly suppressed once  $|\mu|$  increases beyond  $0.9 \text{ eV}$  (the onset of the second subband). The maximum power factor occurs near the onset of the second subband. Remarkable  $ZT_e$  values are observed at  $|\mu|$  near  $0.9 \text{ eV}$  in Fig. 4(d). Here, we have omitted  $\kappa_{ph}$  in the calculation of  $ZT_e$ . This implies that finding a mechanism to reduce  $\kappa_{ph}$  to a value below  $\kappa_e$  is important in the realization of high-efficiency thermoelectric materials.<sup>2)</sup>

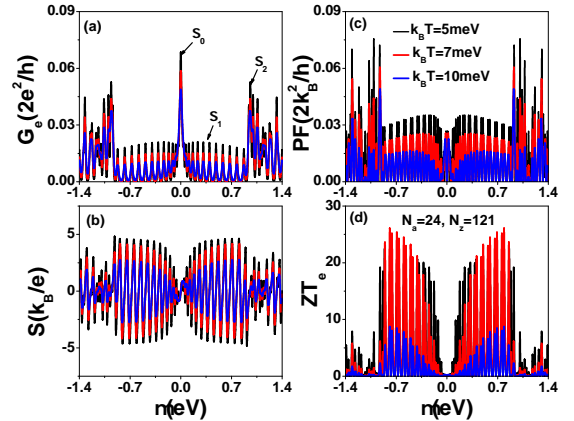


FIG. 4: (a) Electrical conductance  $G_e$ , (b) Seebeck coefficient  $S$ , (c) power factor  $PF$  and (d) figure of merit,  $ZT_e$  as functions of  $\mu$  for GNRs with  $N_z = 121$  ( $L_z = 14.76 \text{ nm}$ ) and  $N_a = 24$  ( $L_a = 2.41 \text{ nm}$ ).  $\gamma_L = \gamma_R = 9 \text{ meV}$ .

### 2. Graphene nanoribbons with $N_a \gg N_z$

Unlike  $G_e$  (which prefers band-like situation), the best  $S$  comes from discrete electronic states (atomic-like situation). Therefore, we consider the situation of  $N_a \gg N_z$  to make the  $\Sigma_0$  peak (due to edge states) well separated from the higher subband states. Figure 5 shows  $G_e$  as a function of  $\mu$  for GNRs with  $N_a = 100$  and  $N_z = 10, 15$ , and  $20$  (corresponding to  $L_z = 1.1, 1.72$  and  $2.34 \text{ nm}$ ), at

zero temperature. Here, the GNRs with  $N_z = 10$ , and 15 are semiconducting, while the GNR with  $N_z = 20$  is metallic. For the semiconducting phase, a sizable gap opens up between the conduction band and valence band. Most importantly, the zigzag edge state appears at the mid gap (the peak marked  $\Sigma_0$ ) as can be seen in Fig. 5(a,b). We note that there are two zigzag edge states localized at the top and bottom ends of the GNR. The charge density of GNRs provided in Fig. B.1 reveal that these zero-energy modes are derived from zigzag edge states. Obviously, the variation of  $N_z$  not only changes the phase of GNRs but also the magnitude and width of  $\Sigma_0$ . Such a phenomenon does not exist in infinite long AGNRs.<sup>46,47)</sup>

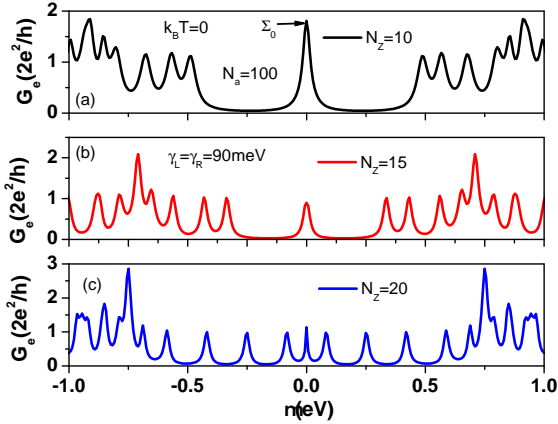


FIG. 5: Electrical conductance as functions of  $\mu$  for various  $N_z$  numbers at  $k_B T = 0$  and  $N_a = 100$ .  $\gamma_L = \gamma_R = 90$  meV.

Mahan and Sofo proposed to employ a single quantum dot (QD) to realize a Carnot heat engine.<sup>48)</sup> The  $G_e$  spectra near  $\mu = 0$  shown in Fig. 5(a,b) are similar to the  $G_e$  spectra of nanoscale semiconductor QDs. To further clarify the effect of zero-energy modes on thermoelectric coefficients, we show the calculated  $G_e$ ,  $S$ ,  $PF$  and  $\kappa_e$  as functions of  $\mu$  for the case with  $N_z = 15$  (Fig. 5(b)) at  $k_B T = 9$  meV in Fig. 6. The electrical conductance due to zigzag edge states ( $\Sigma_0$ ) is suppressed with increasing temperature. Such a behavior is very common in a single QD system. The maximum Seebeck coefficient  $S_{h(e),0,max}$  resulting from  $\Sigma_0$  depends on the gap around the  $\Sigma_0$  peak ( $\Delta = E_c - E_v$ ) (or see Fig. 7). Although the maximum  $PF_{0,max}$  arising from zero energy modes is slightly smaller than  $PF_{B,max}$  resulting from bulk states, its electron thermal conductance could be very small. This indicates that the thermoelectric efficiency of zero energy modes is better than that of bulk states.

Next we examine the size effect of  $N_z$  on thermoelectric quantities. We show the calculated  $G_e$ ,  $S$ ,  $PF$  and the figure of merit ( $ZT_e = S^2 G_e T / \kappa_e$ ) as functions of  $\mu$  for different values of  $N_z$  at  $k_B T = 27$  meV (near room temperature) for the case with a smaller tunneling rate

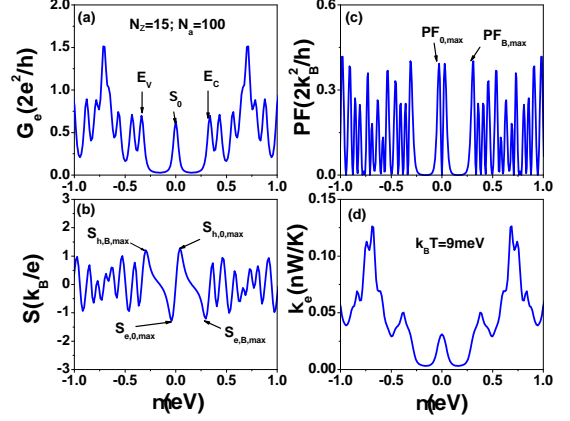


FIG. 6: (a) Electrical conductance  $G_e$ , (b) Seebeck coefficient  $S$ , (c) power factor  $PF$  and (d) electron thermal conductance  $\kappa_e$  as functions of  $\mu$  for various temperatures at  $N_a = 100$ , and  $N_z = 15$ .  $\gamma_L = \gamma_R = 90$  meV.

( $\gamma_L = \gamma_R = 9$  meV) in Fig. 7. We kept  $N_z = 3m$  ( $m$  is an integer) in Fig. 7 to maintain a finite band gap for GNRs. As seen in Fig. 7(a), the electrical conductance  $\Sigma_0$  is reduced with increasing  $N_z$  (also see Fig. 5). In addition, the maximum  $S_0$  value is degraded with the increase of  $N_z$  since the nearest peaks get close to  $\Sigma_0$ . It is worth noting that the behavior of  $S_0 = \mu / (eT)$  is observed in Fig. 7(b). Such a feature was theoretically reported in our previous study.<sup>49)</sup> Meanwhile, the maximum  $PF$  and  $ZT$  occur at the condition with  $|\mu| / (k_B T) = 2.4$ . In the calculation of  $ZT_e$ , we have considered  $\kappa_{ph} = 0$  to estimate the maximum  $ZT$  values. If instead we adopted  $\kappa_{ph} = \frac{\pi^2 k_B^2 T}{3h}$ ,<sup>28,45)</sup>  $ZT$  will reduce significantly. In Fig. 7, we have adopted  $\gamma_{L(R)} = 9$  meV, which is one order of magnitude smaller in comparison with cases considered in figures(5) and (6). Tunneling rates could be affected by the Schottky barrier contact between metal and semiconductor.<sup>50)</sup>

It will be a big challenge to make  $\kappa_{ph}$  much smaller than  $\kappa_e$  in the situation of  $N_a \gg N_z$ . Due to a short channel length ( $L_z = 1.72$  nm), both electrons and phonons remain in the ballistic transport regime. Nevertheless, the zero-energy modes resulting from zigzag edge states are very robust. The transport of zero energy modes of GNRs are topologically protected against scattering while phonons are significantly scattered when defects or disorders are introduced into the transport system. As a consequence,  $\kappa_{ph}$  is highly reduced.<sup>51)</sup> So far, a quantitative study on how defects influence the electron transport through zigzag-edge states in finite-size GNRs is still lacking.<sup>52)</sup>

To examine how robust the  $\Sigma_0$  peak resulting from zigzag edge states is against the presence of defects,<sup>51,52)</sup> we show in Fig. 8 the effect on  $G_e$  due to atomic vacancies randomly distributed in GNRs. We plot  $G_e$  as a func-



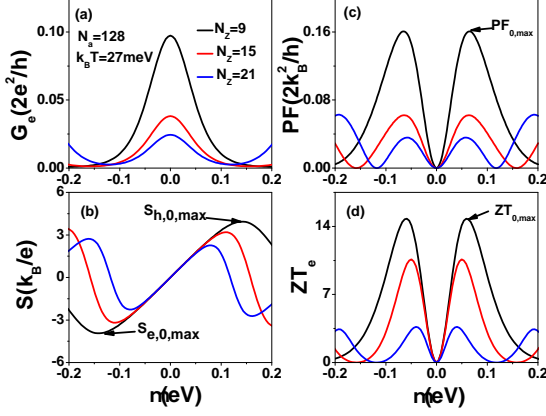


FIG. 7: (a) Electrical conductance, (b) Seebeck coefficient, (c) power factor and (d) figure of merit ( $ZT_e$ ) as functions of chemical potential for different  $N_z$  values at  $N_a = 128$  ( $L_a = 13.49\text{nm}$ ),  $k_B T = 27\text{meV}$  and  $\gamma_L = \gamma_R = 9\text{meV}$ .

tions of  $\mu$  for different defect locations at  $k_B T = 27\text{meV}$  and  $\gamma_{L(R)} = 27\text{meV}$  for finite-size GNRs with  $N_z = 9$  ( $L_z = 0.98\text{nm}$ ) and  $N_a = 128$  ( $L_a = 13.49\text{nm}$ ). We use the concept of orbital removal (by setting the energy level of the defect site to a large value  $E_d = 1000\text{eV}$ ) to mimic the creation of a vacancy. Fig. 8(a) shows that when the vacancy occurs at any location ( $\ell, j$ ) away from the zigzag edge (with  $\ell > 1$  or  $\ell < N_a$ )  $G_e$  of the GNR is almost the same as the defect-free (DF) case, where the peak height of  $G_e$  is close to  $0.24G_0$ . On the other hand, when a vacancy occurs on one zigzag edge (with  $\ell = 1$  or  $\ell = N_a$ ) the conductance  $G_e$  reduces by  $1/2$ , indicating the contribution to the electron transport by the zero-energy mode at that edge is blocked by the presence of vacancy, the contribution due the other edge remains intact. As shown in Fig. 8(b), the effect of defects on the behavior of power factor is quite similar to that of  $G_e$ . This indicates that Seebeck coefficient,  $S_0$  resulting from zigzag-edge states is essentially unchanged against defect scattering. This means that  $S_0$  will not reduce appreciably even though a vacancy blocks the transport on one zigzag edge. Vacancies away from the zigzag edge won't influence the  $\Sigma_0$  peak and  $S_0$  spectrum, but they are expected to reduce  $\kappa_{ph}$  significantly, thus improving the figure of merit  $ZT$ .<sup>51)</sup>

The contact problem between metal and semiconductor plays a remarkable role in the novel applications of 2D electronics.<sup>50)</sup> Here, we show that the tunneling rate ( $\gamma_{L,R}$ ), which depends on the contact property, can significantly affects the thermoelectric properties of GNRs. The calculated electrical conductance, Seebeck coefficient, power factor and figure of merit as functions of chemical potential for various tunneling rate  $\gamma_L = \gamma_R$  at  $k_B T = 27\text{meV}$  are shown in Fig. 9(a)-(d). From results of Fig. 9(a), we see that it is not easy to mea-

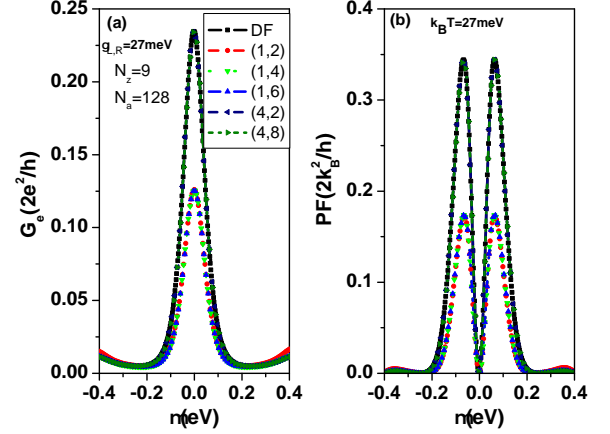


FIG. 8: (a) Electrical conductance and (b) power factor as functions of chemical potential for different defect locations at  $k_B T = 27\text{meV}$ ,  $\gamma_{L(R)} = 27\text{meV}$ ,  $N_z = 9$  and  $N_a = 128$  ( $L_a = 13.49\text{nm}$ ).

sure  $\Sigma_0$  peak when  $\gamma_{L,R}/(2k_B T) \ll 1$ . In contrast to  $G_e$ ,  $S_0$  prefers weaker coupling strength between metal and GNR. Although  $S_0$  can be improved by reducing  $\gamma_{L,R}$ , the electrical power output of GNRs is greatly enhanced as  $\gamma_{L,R}$  increases. Combining the above considerations we found that the maximum  $ZT$  occurs when the tunneling rate matches the operating temperature, i.e.  $\gamma_{L,R} = k_B T$ , when the phonon thermal conductivity is included. Here, we have adopted  $\kappa_{ph} = F_s \frac{\pi^2 k_B^2 T}{3h}$ , where  $F_s = 0.1$  is a reduction factor due to phonon scattering with defects in nanoscale GNRs.<sup>45,53)</sup> Obviously, the optimization of  $ZT$  at finite  $\kappa_{ph}$  situation is different from the case with  $\kappa_{ph} = 0$  (see Fig. 7).

#### IV. CONCLUSION

We have theoretically investigated the transport and thermoelectric properties of GNRs with zigzag and armchair edges in the framework of Green's function approach within a tight-binding model. GNRs can have sophisticated metallic or semiconducting phases depending on the nanoribbon width. We clarified quantum confinement effect on the transport and thermoelectric properties of GNRs. In particular, we found that the confinement effect of ZGNRs can highly enhance the Seebeck coefficient at low temperature. When the zigzag sides are coupled to the electrodes, electron transport through localize zigzag states can be resolved only when the armchair length is smaller than the decay length of zigzag edge states along armchair direction. For GNRs in semiconducting phase in which the armchair edges are coupled to the electrodes we can get significant electron conductance through the zero-energy modes. For cases with  $N_a \gg N_z$  in Fig. 1(b), the top and bottom zigzag edges

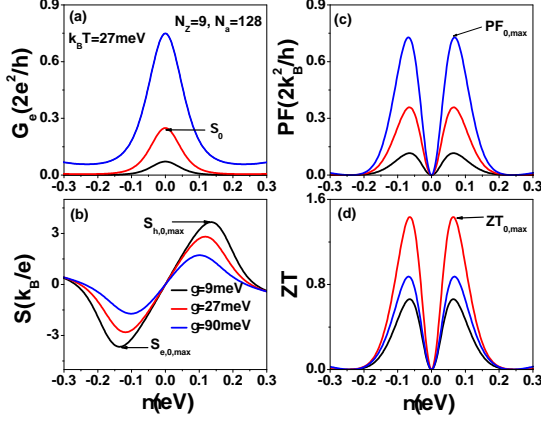


FIG. 9: (a)Electrical conductance, (b)Seebeck coefficient, (c) power factor and (d) figure of merit as functions of chemical potential for different tunneling rate ( $\gamma_{L(R)} = \gamma$ ) values at  $k_B T = 27 \text{ meV}$ ,  $N_z = 9$  and  $N_a = 128$ . Note that  $\kappa_{ph} = F_s \frac{\pi^2 k_B^2 T}{3h}$  and  $F_s = 0.1$ .

are essentially decoupled and the thermoelectric behavior of zero-energy modes can be well described by using two parallel quantum dots with the same orbital degeneracy. Therefore, the optimized  $PF$  and the best  $ZT_e$  of zero energy modes could be analytically obtained in the case of  $\kappa_{ph} = 0$ . We found that  $\Sigma_0$  of zero-energy modes is very robust against the carrier scattering from point defects as long as they do not appear on the edge. This mechanism provides the promising means to reduce  $\kappa_{ph}$  and remains the power factor of  $PF_{0,max}$  resulting from zigzag edge states.

#### Acknowledgments

This work was supported by the Ministry of Science and Technology (MOST), Taiwan under Contract No. 110-2119-M-008-006-MBK. The author thanks Yia-Chung Chang for help with the manuscript preparation and supporting IBM computer clusters.

E-mail address: mtkuo@ee.ncu.edu.tw

### Appendix A: Electronic band structures

Although the electronic band structures of GNRs have been intensively studied,<sup>30–36)</sup> we briefly illustrate the band structure of GRNs here to make this manuscript more readable. Fig. 2 shows the electron transport behavior from the left electrodes to the right electrode via an GNR. Decoupling the electrodes, we calculate the electronic band structures of AGRNs for different  $N_z$  values in Fig. A. 1, which exhibit the semiconducting and metallic phases.  $N_z = 20$  shows a metallic phase.

$N_z = 10, 24, 30$  show semiconducting phases. Due to time-reversal symmetry, electron-hole symmetry exists in Fig. A. 1. The results of Fig. A. 1 could explain the material phases shown in Fig. 2. For the cases of odd  $N_z$  such as  $N_z = 5, 7, 9$  (not shown here), the flat-bands appear at  $E = \pm 2.7 \text{ eV}$ , which agree with analytical solution of AGRNs.<sup>33)</sup>

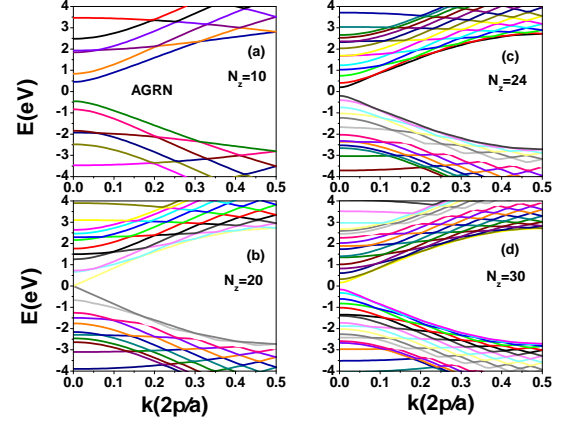


FIG. A.1: Electronic band structures for armchair GRNs for different  $N_z$  values.

The extra peak  $\Sigma_0$  shown in Figures 3 and 4 results from the zigzag edge states. To demonstrate such a feature, we show the electronic band structures of zigzag GNRs for different  $N_a$  values. As seen in Fig. A. 2(d) with  $N_a = 30$ , there are a pair of orbit degeneracy in the flat-bands with zero electron group velocity. This zero energy flat-band modes is from  $k = \frac{2\pi}{3a}$  to  $\frac{\pi}{a}$ . In Ref. [31] authors gave an analytical solution for the large  $N_a$  limit. The results of Fig. A. 2(d) indicate that the zigzag edges are decoupled when  $N_a \geq 30$ . For smaller  $N_a$  values, only  $k = \frac{\pi}{a}$  has zero energy modes. When  $k$  is deviating from  $\frac{\pi}{a}$ , the zigzag edges states form the bonding and antibonding states. Therefore, zero-energy modes are lifted.<sup>31)</sup> Based on the results of Figs. A. 1 and A. 2, we consider finite GNRs with zigzag and armchair edges, which allow GNRs with zero-energy modes protected by the band gap.<sup>46)</sup>

### Appendix B: Charge density

To further reveal the properties of edge states, we calculate the charge density of GNRs, which are determined by the wave functions of finite size GNRs ( $|\psi_{\ell,j}(\varepsilon)|^2$ ). The charge density of GNRs with  $N_a = 100$  and  $N_z = 15$  decoupled with the electrodes is plotted in Fig. B. 1 at various locations inside the GNR with  $(\ell, j)$  (see Fig. 1(a)). The maximum zigzag edge charge density  $|\psi_{\ell,j}(\varepsilon = 0)|^2$  at  $j = 1$  decays quickly with increasing lattice index for  $j$  ( $j=3,5,7,9,11,13,\dots$ ). The results show clear

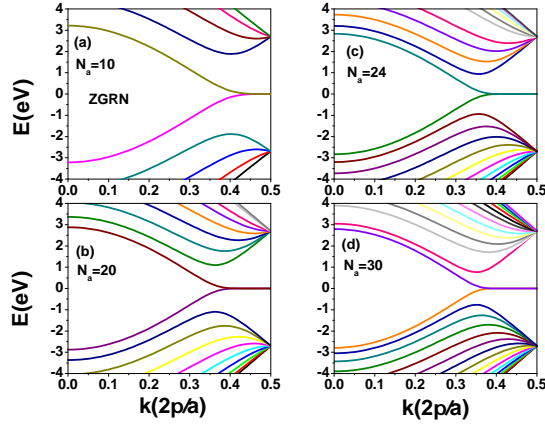


FIG. A.2: Electronic band structures for zigzag GRNs for different  $N_a$  values.

evidence for zero-energy modes resulting from the zigzag-edge states with localized wave functions along armchair edge direction. Such results of Fig. B. 1 explain why we can not observe the zero energy modes in Fig. 2, but observe it in Fig. 3.

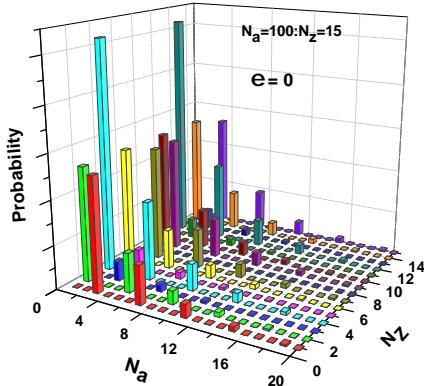


FIG. B.1: Charge density of GNRs with  $N_a = 100$  and  $N_z = 15$ . We plot  $|\psi_{\ell,j}(\varepsilon = 0)|^2$  for  $\ell$  from 1 to 15 and  $j$  from 1 to 20.

Next, the charge density of GNRs with  $N_z = 121$  and  $N_a = 24$  are plotted in Fig. B. 2 at various locations of the GNRs. The maximum zigzag edge charge density occurs at  $j = 1$  and  $j = 24$  for even  $\ell$  numbers. Due to a small  $N_a$  value, the localized edge states ( $\varepsilon = 0.068\text{eV}$ ) form the bond and antibonding states. As seen in Fig. B. (2a), the oscillatory charge density along the direction of zigzag edges. For the case of  $\varepsilon = 0.58\text{eV}$ , the charge density of GNRs shows delocalized wave functions.

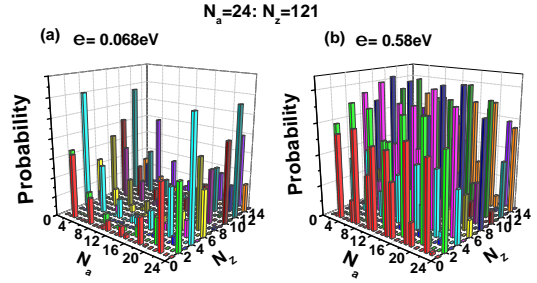


FIG. B.2: Charge density of GNRs with  $N_z = 121$  and  $N_a = 24$ . (a)  $|\psi_{\ell,j}(\varepsilon = 0.068\text{eV})|^2$ , and (b)  $|\psi_{\ell,j}(\varepsilon = 0.58\text{eV})|^2$ .  $\ell$  is accounted from 1 to 14 and  $j$  is from 1 to 24.

- <sup>1)</sup> A. J. Minnich, M. S. Dresselhaus, Z. F. Ren and G. Chen: Energy Environ Sci, **2**, (2009) 466.
- <sup>2)</sup> G. Chen, M. S. Dresselhaus, G. Dresselhaus, J. P. Fleurial, and T. Caillat: International Materials Reviews, **48**, (2003) 45.
- <sup>3)</sup> L. D. Hicks and M. S. Dresselhaus: Phys. Rev. B **47** (1993) 16631.
- <sup>4)</sup> Y. M. Lin and M. S. Dresselhaus: Phys. Rev. B **68**, (2003) 075304.
- <sup>5)</sup> O. Rabina, Y.-M. Lin, and M. S. Dresselhaus: Appl. Phys.

- Lett. **79** (2001) 81.
- <sup>6)</sup> A. Boukai, Y. Bunimovich, J. Tahir-Kheli, J.-K. Yu, W. A. Goddard III, and J. R. Heath: Nature **451** (2008) 168.
- <sup>7)</sup> A. Hochbaum, A. I. Hochbaum, R. Chen, R. D. Delgado, W. Liang, E. C. Garnett, M. Najarian, A. Majumdar, and P. D. Yang: Nature **451** (2008) 163.
- <sup>8)</sup> J. P. Heremans, C. M. Thrush, D. T. Morelli, and M. Wu: Phys. Rev. Lett. **88** (2002) 216801.
- <sup>9)</sup> K. S. Novoselov, A. K. Geim, S. V. Morozov, D. Jiang, Y. Zhang, S. V. Dubonos, I. V. Grigorieva, and A. A. Firsov:



- Science **306** (2004) 666.
- <sup>10)</sup> J. Cai, P. Ruffieux, R. Jaafar, M. Bieri, T. Braun, S. Blankenburg, M. Muoth, A. P. Seitsonen, M. Saleh, X. Feng, K. Mullen, and Roman Fasel: Nature **466**, (2010) 470.
  - <sup>11)</sup> L. Brey and H. A. Fertig: Phys. Rev. B **73**, (2006) 235411.
  - <sup>12)</sup> A. K. Geim, and I. V. Grigorieva: Nature **499**, (2013) 419.
  - <sup>13)</sup> K. S. Novoselov, A. Mishchenko, A. Carvalho, and A. H. C. Neto: Science **353**, (2016) aac9439.
  - <sup>14)</sup> S. Manzeli, D. Ovchinnikov, D. Pasquier, O. V. Yazyev and A. Kis: Nature Reviews Materials **2**, (2017) 17033.
  - <sup>15)</sup> X. F. Qian, J. W. Liu, L. Fu, and J. Li: Science **346**, (2014) 1344.
  - <sup>16)</sup> X. M. Wang, A. M. Jones, K. L. Seyler, V. Tran, Y. C. Jia, H. Zhao, H. Wang, L. Yang, X. D. Xu, and F. N. Xia, Nature: Nanotechnology **10**, (2015) 517.
  - <sup>17)</sup> Y. Wang, J. Xiao, H. Y. Zhu, Y. Li, Y. Alsaïd, K. Y. Fong, Y. Zhou, S. Q. Wang, W. Shi, Y. Wang, A. Zettl, E. J. Reed, and X. Zhang: Nature **550**, (2017) 487.
  - <sup>18)</sup> A. Y. Lu, H. Y. Zhu, J. Xiao, C. P. Chuu, Y. M. Han, M. H. Chiu, C. C. Cheng, C. W. Yang, K. H. Wei, Y. M. Yang, Y. Wang, D. Sokaras, D. Nordlund, P. D. Yang, D. A. Muller, M. Y. Chou, X. Zhang and L. J. Li: Nature: Nanotechnology **12**, (2017) 744.
  - <sup>19)</sup> L. Z. Kuo, Y. D. Ma, Z. G. Sun, T. Heine and C. F. Chen: J. Phys. Chem. Lett. **8**, (2017) 1905.
  - <sup>20)</sup> T. Olsen, T. Okugawa, D. Torelli, T. Deilmann, and K. S. Thygesen: Phys. Rev. Materials **3**, (2019) 024005.
  - <sup>21)</sup> X. Cai, X. Han, C. X. Zhao, C. Y. Niu and Y. Jia: J. Semiconductors, **41**, (2020) 081002.
  - <sup>22)</sup> Z. Guo, D. Zhang and X. G. Gong: Appl. Phys. Lett. **95**, (2009) 163103.
  - <sup>23)</sup> L. Xian, A. PerezPaz, E. Bianco, P. M. Ajayan and A. Rubio: 2D material. **4**, (2017) 041003.
  - <sup>24)</sup> S. Sharma, N. Singh and U. Schwingenschlogl: Appl. Energy Mater. **1**, (2018) 1950.
  - <sup>25)</sup> C. H. Lin, W. D. Cheng, G. L. Chai and H. Zhang: Phys. Chem. Chem. Phys. **20**, (2018) 24250.
  - <sup>26)</sup> D. V. Kosynkin, A. L. Higginbotham, A. Sinitskii, J. R. Lomeda, A. Dimiev, B. K. Price, and J. M. Tour: Nature **458**, (2009) 872.
  - <sup>27)</sup> L. Jiao, L. Zhang, X. Wang, G. Diankov, and H. Dai: Nature **458** (2009) 877.
  - <sup>28)</sup> Y. Xu, X. B. Chen, B. L. Gu and W. H. Duan: Appl. Phys. Lett. **95**, (2009) 233116.
  - <sup>29)</sup> T. Kato, S. Usui, and T. Yamamoto: Jap. J. Appl. Phys. **52** (2013) 06GD05.
  - <sup>30)</sup> M. Fujita, K. Wakabayashi, K. Nakada, and K. Kusakabe: J. Phys. Soc. Jpn. **65** (1996) 1920.
  - <sup>31)</sup> K. Nakada, M. Fujita, G. Dresselhaus and M. S. Dresselhaus: Phys. Rev. B **54**, (1996) 17954.
  - <sup>32)</sup> K. Wakabayashi, M. Fujita, H. Ajiki, and M. Sigrist: Phys. Rev. B **59**, (1999) 8271.
  - <sup>33)</sup> H. Zheng, Z. F. Wang, T. Luo, Q. W. Shi and Jie Chen: Phys. Rev. B **75**, (2007) 165414.
  - <sup>34)</sup> W. Jaskolski, A. Ayuela, M. Pelc, H. Santos, and L. Chico: Phys. Rev. B **83**, (2011) 235424.
  - <sup>35)</sup> Y. W. Son, M. L. Cohen, and Steven G. Louie: Phys. Rev. Lett. **97**, (2006) 216803.
  - <sup>36)</sup> Y. W. Son, M. L. Cohen and Steven G. Louie: Nature **444**, (2006) 347.
  - <sup>37)</sup> P. Shemella, Y. Zhang, M. Mailman, P. M. Ajayan, and S. K. Nayak: Appl. Phys. Lett. **91**, (2007) 042101.
  - <sup>38)</sup> O. Hod, J. E. Peralta, and G. E. Scuseria: Phys. Rev. B **76**, (2007) 233401.
  - <sup>39)</sup> Y. Hernandez-Espinosa, R. A. Mendez-Sanchez and E. Sadurni, J. Phys. B: At. Mol. Opt. Phys. **53** (2020) 105101.
  - <sup>40)</sup> H. Haug and A. P. Jauho, Quantum Kinetics in Transport and Optics of Semiconductors (Springer, Heidelberg, 1996).
  - <sup>41)</sup> D. M. T. Kuo, C. C. Chen and Y. C. Chang: Phys. Rev. B **95**, (2017) 075432.
  - <sup>42)</sup> Y. Meir and N. S. Wingreen: Phys. Rev. Lett. **68**, (1992) 2512.
  - <sup>43)</sup> D. M. T. Kuo: AIP Advances **10**, (2020) 045222.
  - <sup>44)</sup> Y. F. Zhou, H. Jiang, X. C. Xie and Q. F. Sun: Phys. Rev. B **95**, (2017) 245137.
  - <sup>45)</sup> T. Yamamoto and K. Watanabe: Phys. Rev. Lett. **96**, (2006) 255503.
  - <sup>46)</sup> L. Malysheva and A. Onipko: Phys. Rev. Lett. **100**, (2008) 186806.
  - <sup>47)</sup> K. Wakabayashi, K. Sasaki, T. Nakanishi and T. Enoki: Sci. Technol. Adv. Mater. **11** (2010) 054504.
  - <sup>48)</sup> G. D. Mahan and J. O. Sofo: Proc. Natl. Acad. Sci. USA **93**, (1996) 7436.
  - <sup>49)</sup> D. M. T. Kuo and Y. C. Chang: Phys. Rev. B **81**, (2010) 205321.
  - <sup>50)</sup> P. C. Shen, C. Su, Y. X. Lin, A. S. Chou, C. C. Cheng, J. H. Park, M. H. Chiu, A. Y. Lu, H. L. Tang, M. M. Tavakoli, G. Pitner, X. Ji, X. Z. Y. Cai, N. N. Mao, J. T. Wang, V. C. Tung, J. Li, J. Bokor, A. Zettl, C. I. Wu, T. Palacios, L. J. Li, and J. Kong: Nature **593**, (2021) 211.
  - <sup>51)</sup> Y. Xu, Z. Gan, and S. C. Zhang: Phys. Rev. Lett. **112**, (2014) 226801.
  - <sup>52)</sup> T. C. Li and Shao-Ping Lu: Phys. Rev. B **77**, (2008) 085408.
  - <sup>53)</sup> H. Zheng, H. J. Liu, X. J. Tan, H. Y. Lv, L. Pan, J. Shi, and X. F. Tang: Appl. Phys. Lett. **100**, (2012) 093104.